PAPER

Check for updates

A novel mixed-conducting network in all-oxide composites: overcoming traditional percolation constraints†

Fanlin Zeng, [ID] *[a] Ke Ran, [ID] [bc] Christian Dellen, [ID] [a] Hartmut Schlenz,[a]
Joachim Mayer,[bc] Ruth Schwaiger,[ade] Wilhelm Albert Meulenberg [ID] [af]
and Stefan Baumann [ID] [a]

Mixed-conducting composites play pivotal roles in ceramic devices for advancing efficient and environment-friendly energy consumption and conversion processes. Conventionally, these materials are synthesized *via* the blending of distinct conducting phases, where grain percolation of each phase is considered essential. This approach inevitably leads to intertwined networks interspersed with inactive regions, limiting the overall performance. This study challenges this conventional paradigm by proposing an alternative percolation mechanism that circumvents the need for strict grain connectivity. The mechanism is demonstrated in composites of doped ceria with iron–cobalt oxide additives, where grains of the doped ceria constitute over 80 vol% and are nearly completely percolated for efficient and rapid ionic conduction. Remarkably, even though the additive-induced electronic conducting grains occupy less than 20 vol% and are distributed as islands, the observed electronic conductivity far surpasses conventional predictions. This anomaly is attributed to the accumulation of charge carriers at ceria grain boundaries, which facilitates electronic conduction. Through extensive structural and compositional analyses at micro- and nanoscale levels, the study unveils novel insights into the intricate architecture of this advanced percolation network. Furthermore, the optimization of these composites is achieved by enriching iron and cobalt cations at ceria grain boundaries, while inhibiting grain coarsening. This delicate balance culminates in excellent and sustainable mixed conductivity for oxygen permeation, thus advancing the potential of mixed-conducting composites for applications in clean and efficient energy technologies.

Introduction

Mixed ionic and electronic conducting materials are indispensable in deploying electrochemical ceramic devices to supplant high carbon-emitting industrial processes and facilitate energy conversion from green sources.[1,2] For instance, these materials are widely applied as dense membranes in catalytic membrane reactors for partial oxidation of hydrocarbons,[3]

[a]*Forschungszentrum Jülich GmbH, Institute of Energy Materials and Devices (IMD), Jülich, 52425, Germany. E-mail: f.zeng@fz-juelich.de*

[b]*Central Facility for Electron Microscopy GFE, RWTH Aachen University, 52074 Aachen, Germany*

[c]*Ernst Ruska-Centre for Microscopy and Spectroscopy with Electrons (ER-C), Forschungszentrum Jülich GmbH, 52425 Jülich, Germany*

[d]*RWTH Aachen University, Chair of Energy Engineering Materials, Aachen, 52056, Germany*

[e]*Jülich Aachen Research Alliance, JARA-Energy, Jülich, 52425, Germany*

[f]*University of Twente, Faculty of Science and Technology, Inorganic Membranes, P. O. Box 217, Enschede, 7500 AE, The Netherlands*

† Electronic supplementary information (ESI) available. See DOI: https://doi.org/10.1039/d4ta06889k

hydrogen purification,[4] and water splitting,[5,6] as well as porous electrodes in solid oxide fuel cells (SOFCs) for green power conversion.[7]

Perovskite oxide compounds such as $Ba_{0.5}Sr_{0.5}Co_{0.8}Fe_{0.2}O_{3-\delta}$ and $La_{0.6}Sr_{0.4}Co_{0.2}Fe_{0.8}O_{3-\delta}$ are widely recognized for their excellent mixed ionic and electronic conductivity.[8,9] However, these materials suffer from poor chemical and dimensional stability in application-relevant atmospheres involving CO_2, H_2O, CH_4, H_2S, and/or SO_2.[10,11]

By contrast, the fluorite-type compounds, such as ZrO_2 stabilized by Y or/and Sc,[12–14] as well as CeO_2 doped with trivalent rare earth elements (Gd, Sm, and Nd), demonstrate superior chemical compatibility with corrosive gas species.[15,16] Unfortunately, Y- or Sc-stabilized ZrO_2 shows negligible electronic conductivity within the application temperature range of 800–1000 °C.[17] Similarly, trivalent lanthanide (Gd, Sm, and Nd) doped CeO_2 functions predominantly as a pure ionic conductor across a broad range of oxygen partial pressure from 0.21 atm to $\sim10^{-15}$ atm in the same temperature window.[18] To introduce mixed conductivity in CeO_2, lanthanide dopants with mixed valence states, *e.g.*, Pr and Tb, can be utilized.[19–21] In addition,

14940 | *J. Mater. Chem. A*, 2025, **13**, 14940–14956

This journal is © The Royal Society of Chemistry 2025

the electronic conductivity can be enhanced by adding a single or binary oxide containing redox-active transition metal element(s).[22–27] At sufficiently high concentrations, these additives form an interconnected grain network supporting substantial electronic conductivity. However, excessive additive content leads to a volumetric dilution of the fluorite matrix and disrupts the contiguity of fluorite grains,[28] both of which are detrimental to the already sluggish ionic conduction. Thus, it is essential to minimize the additive content while ensuring effective electronic percolation. Experimental findings suggest that even a minor addition (∼2 mol%) of Fe, Co or Cu cations to doped CeO_2 can feasibly induce p-type electronic conduction under air condition.[29,30]

These additives do not form separate electronic conducting grains but predominantly segregate at ceria grain boundaries, existing as point defects or a thin amorphous layer.[30,31] In this case, the electron/hole conduction occurs along ceria grain boundaries, as illustrated by schematic I in Fig. 1(a). The corresponding electronic conductivity (line I in Fig. 1(b)) for 2 mol% Co-modified $Ce_{0.8}Gd_{0.2}O_{2-\delta}$ exhibits a high activation energy and remains approximately an order of magnitude lower than the ionic conductivity.[29] Consequently, the resultant electronic conductivity is insufficient for high-performance electrochemical applications, particularly when compared to CeO_2 doped with mixed-valence cations such as Pr. A likely cause is the low concentration of charge carriers at ceria grain boundaries.

An alternative and underexplored composite architecture is proposed herein, as illustrated by schematics II and III in Fig. 1(a). In this structure, the transition metal oxide additive(s) not only forms islands of electronic conducting grains within the ceria matrix but also decorates ceria grain boundaries with transition metal element(s). This configuration enables ceria grain boundaries to act as an "electronic conducting shuttle" between adjacent electronic conducting grains. As compared to the system in schematic I where ceria grain boundaries serve as the sole electronic conducting channels, this arrangement can offer physically shortened paths for electrons/holes along ceria grain boundaries without blocking ionic conduction pathways across ceria grain boundaries. However, experimental results reveal striking conductivity differences between two similar structure representatives: 80 vol% $Ce_{0.8}Gd_{0.2}O_{2-\delta}$–20 vol% $CoFe_2O_4$ (ref. 27) and 81.5 vol% $Ce_{0.8}Gd_{0.2}O_{2-\delta}$–18.5 vol% $FeCo_2O_4$.[16] Their electronic conductivities, plotted as lines II and III in Fig. 1(b), differ by over two orders of magnitude. The 20 vol% $CoFe_2O_4$ additives fail to overcome the electronic conductivity bottleneck of $Ce_{0.8}Gd_{0.2}O_{2-\delta}$. A likely cause is the insufficient transition metal segregation at ceria grain boundaries (schematic II in Fig. 1(a)), which results in highly tortuous electronic conducting paths. By contrast, the addition of 18.5 vol% $FeCo_2O_4$ leads to enriched transition metal segregation at ceria grain boundaries (schematic III in Fig. 1(a)),[33] significantly accelerating electronic transport along ceria grain boundaries.[16]
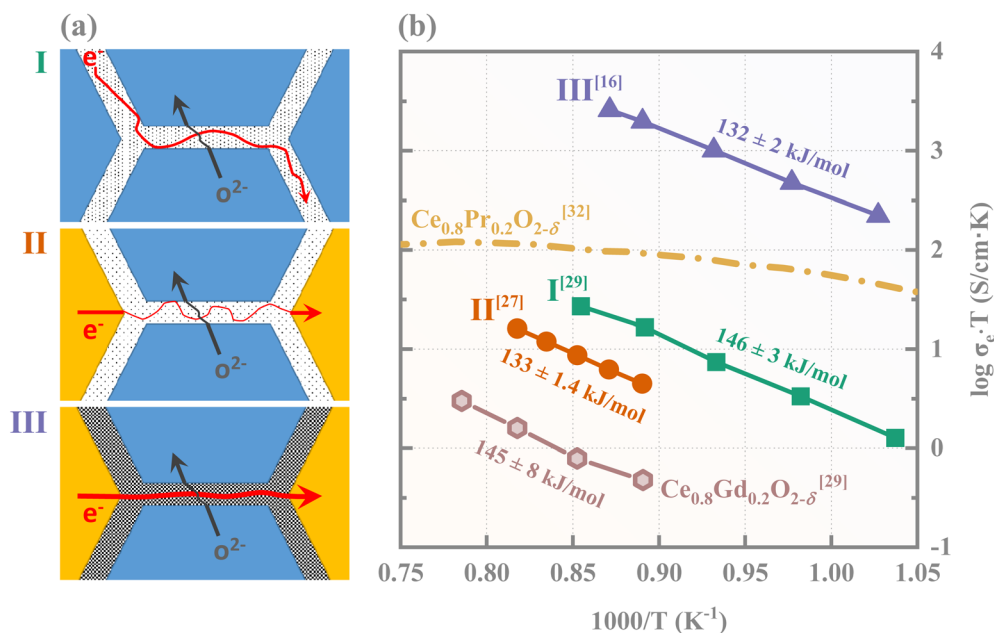

Fig. 1 Schematic illustrations (a) and the corresponding electronic conductivities (b) of microstructural configurations where ceria grain boundaries serve as critical pathways for mixed ionic and electronic conduction. In (a), blue and yellow polygons represent grains of the ionic and electronic conductor, respectively, with intergranular gaps denoting grain boundaries. Black dots of varying densities indicate charge carriers at different concentrations. Red and black line arrows represent electronic and ionic pathways, respectively, with thicker ones signifying faster transport and thinner ones indicating slower conduction. In (b), lines I, II, and III correspond to the electronic conductivities of 2 mol% Co-modified $Ce_{0.8}Gd_{0.2}O_{2-\delta}$,[29] 20 vol% $CoFe_2O_4$–80 vol% $Ce_{0.8}Gd_{0.2}O_{2-\delta}$,[27] and 18.5 vol% $FeCo_2O_4$–81.5 vol% $Ce_{0.8}Gd_{0.2}O_{2-\delta}$,[16] respectively. The electronic conductivity values of line II are estimated to be equal to ambipolar conductivities, given that the ionic conductivity values are approximately one order of magnitude higher.[27] For comparison, the electronic conductivity values of pure $Ce_{0.8}Gd_{0.2}O_{2-\delta}$[29] and $Ce_{0.8}Pr_{0.2}O_{2-\delta}$[32] are also presented. The respective activation energies, expressed in kJ mol^{-1}, are annotated next to the plotted data.

This journal is © The Royal Society of Chemistry 2025

J. Mater. Chem. A, 2025, **13**, 14940–14956 | **14941**

Given these findings, further optimization of this composite architecture is imperative to maximize concurrent ionic and electronic conduction. The network geometry and ceria grain boundary composition are expected to have critical effects. To the best of our knowledge, the impact of network geometry has not yet been thoroughly investigated and discussed. While the ceria grain boundary composition is known to govern electronic percolation, its precise modulation and characterization have proven challenging. Additionally, its influence on ionic conductivity remains unclear.

In this work, we systematically address these open questions and challenges using $FeCo_2O_4$ modified $Ce_{0.8}Gd_{0.2}O_{2-\delta}$ mixed conductors as a model system. The $FeCo_2O_4$ content is limited to 15 wt% ($\sim$19.05 vol% or $\sim$11.44 mol%), *i.e.*, a concentration insufficient for realizing grain percolation. Notably, these two components exhibit strong chemical interactions, leading to the formation of a new electronic conducting $GdFeO_3$-type perovskite, in which Ce substitutes for Gd and Co for Fe.[16,28,34,35] This strong interaction provides an excellent opportunity to tailor grain boundary composition and properties. Our results demonstrated that sintering conditions significantly influence the grain boundary structure and segregation. We further introduce a novel approach, wherein Gd_2O_3 as an additional Gd source is incorporated to enhance phase interactions and optimize the grain boundary environment.

To elucidate the fundamental mechanisms governing mixed conduction, grain boundary characterization is performed at the nanoscale using scanning transmission electron microscopy, combined with energy-dispersive X-ray spectroscopy. Microscale analysis is conducted using scanning electron microscopy and electron backscatter diffraction to quantitatively assess the microstructural evolution and geometric effects on conduction pathways. Finally, the advances in grain arrangement and grain boundary composition in mixed ionic and electronic conduction are evaluated through electrochemical impedance spectroscopy and performance testing in oxygen separation/purification applications.

Experimental

Material preparation

The $FeCo_2O_4$ modified $Ce_{0.8}Gd_{0.2}O_{2-\delta}$ (FC-CGO) mixed conductors were synthesized *via* a solid-state reactive sintering process,[34,36] wherein 85 wt% of $Ce_{0.8}Gd_{0.2}O_{2-\delta}$ (Treibacher Industrie AG, 99%) was ball-milled in ethanol with 15 wt% $FeCo_2O_4$. The latter was prepared from a raw material mixture of Fe_2O_3 (Merck, 99%) and Co_3O_4 (Merck, 99%) in a 3:4 mole ratio. Although $FeCo_2O_4$ spinel was not pre-synthesized, high-temperature XRD analysis revealed that a complete chemical reaction between Co_3O_4 and Fe_2O_3 occurs at $\sim$900 °C, yielding $FeCo_2O_4$ spinel.[36] The dried and sieved powders were pressed into pellets at $\sim$19 MPa and densified after a single-step heating in air at a rate of 3 K min^{-1} to either 1050 °C or 1200 °C for 10 h. Details of sample preparation and treatment that are not specific here can be found in a previous study.[36] The samples are denoted as FC-CGO_LT and FC-CGO_HT, with "LT" and

"HT" referring to the sintering temperature of 1050 °C and 1200 °C, respectively.

To promote phase interaction, the total Gd content in the FC-CGO powder was further increased by adding Gd_2O_3 (Sigma-Aldrich, 99.9%) until the overall Gd/Ce ratio from 2:8 to 3:7. This resulted in a composition of approximately 8.1 wt% Gd_2O_3, 13.8 wt% $FeCo_2O_4$, and 78.1 wt% $Ce_{0.8}Gd_{0.2}O_{2-\delta}$. The same synthesis procedures were then applied to this composition, and the resulting sample is referred to as FCG-CGO_HT.

Additionally, four other conductors were synthesized for comparison analysis. A pure ionic conductor (IC), sintered from $Ce_{0.8}Gd_{0.2}O_{2-\delta}$ with minor Fe_2O_3 addition, represents the fluorite-type ionic conducting phase resulting from phase interaction in the $FeCo_2O_4$ modified $Ce_{0.8}Gd_{0.2}O_{2-\delta}$ composites.[28]

A pure electronic conductor (EC), synthesized as a composite containing spinel, rock-salt, and perovskite phases, represents the collective performance of all electronic conducting phases present in the $FeCo_2O_4$ modified $Ce_{0.8}Gd_{0.2}O_{2-\delta}$.[28]

Two mixed conductors (40FC-CGO_HT and CF-CGO_HT) were prepared from 40 wt% $FeCo_2O_4$–60 wt% $Ce_{0.8}Gd_{0.2}O_{2-\delta}$ and 15 wt% $CoFe_2O_4$–85 wt% $Ce_{0.8}Gd_{0.2}O_{2-\delta}$, respectively.

The preparation steps for these additional samples are detailed in ESI Note 1.†

Phase and microstructure investigation

Microstructural characterization and phase analysis were performed on polished sample cross-sections using scanning electron microscopy (SEM; Merlin, Carl Zeiss Microscopy, Oberkochen, Germany) and electron backscatter diffraction (EBSD; NordlysNano, Oxford Instruments, Wiesbaden, Germany). The volume fraction of each phase was estimated by assuming area fraction equivalence,[37] determined *via* image analysis using the HKL Channel 5 software package based on the EBSD results. Grain percolation and tortuosity calculations were performed using the open-source toolkit PoreSpy.[38]

Grain boundary characterization

Cross-sectional samples were prepared *via* focused ion beam (FIB) milling using a FEI Strata 400 system equipped with Ga ion beam. Further thinning and cleaning were applied to the lamellas using an Ar ion beam in a Fischione Nanomill 1040 at 900 eV and 500 eV beam energy, respectively. Transmission electron microscopy (TEM) and energy-filtered TEM (EFTEM) imaging were conducted using a FEI Tecnai F20 at 200 kV. High resolution high-angle annular dark-field (HAADF) imaging, energy-dispersive X-ray spectroscopy (EDXS) chemical mapping, and electron energy loss spectroscopy (EELS) spectrum imaging were performed using a FEI Titan G2 80-200 ChemiSTEM microscope. This system was equipped with an XFEG, a probe Cs corrector, a Super-X EDXS system, and a Gatan Enfinium ER (model 977) spectrometer with DUAL EELS acquisition capability.[39] A convergence semi-angle of 22 mrad was approximated for scanning transmission electron microscopy (STEM) imaging and EDXS mapping with a typical time of around 10 minutes. Background subtraction was applied to improve signal clarity.

14942 | *J. Mater. Chem. A*, 2025, **13**, 14940–14956

This journal is © The Royal Society of Chemistry 2025

The collection semi-angles were 80–220 mrad for HAADF imaging. The image quality was enhanced by application of an iterative rigid alignment algorithm, followed by smoothing using a non-linear filtering algorithm.[40]

Performance assessment

The material performance was assessed *via* total conductivity measurements and oxygen permeation experiments.

Total conductivity (σ_{tot}), defined as the sum of ionic (σ_i) and electronic conductivity (σ_e) (see eqn (1)), was measured under air and argon (Ar) conditions using electrochemical impedance spectroscopy (EIS) at frequencies from 0.1 Hz to 10 MHz.

Measurements were conducted every 50 K from 900 °C to 750 °C. Prior to measurements, silver paste was brushed on the polished sample surfaces, and fired at 900 °C for 1 h to form a thin current-collecting silver layer. Each sample was saturated at the target temperature for 1 h before measurement.

$$\sigma_{tot} = \sigma_i + \sigma_e \quad (1)$$

Oxygen permeation was measured using a 4-end in-house built setup. To eliminate surface exchange limitations, the sintered pellets were polished and screen printed with a ~4 μm thick porous $La_{0.58}Sr_{0.4}Co_{0.2}Fe_{0.8}O_{3-\delta}$ coating on both sides.[34,41] The coated pellets were then sealed with gold rings and mounted in glass tubes at ~1020 °C under pressure. One side of each pellet was fed with air at a flow rate of 250 ml min^{-1}, while the other side was swept by Ar at a flow rate of 50 ml min^{-1}. Oxygen flux was recorded at steady-state conditions every 50 °C from ~1000 °C down to ~850 °C, and then normalized by the oxygen partial pressure gradient across the pellet to determine oxygen permeance. If the permeation process is limited by bulk diffusion rather than surface exchange, oxygen permeance can be described by eqn (2).[34,41]

$$\text{Oxygen permeance} = \frac{R}{16F^2} \times \frac{1}{L} \times \sigma_{amb} \times T \quad (2)$$

where σ_{amb} is the ambipolar conductivity, as defined by eqn (3). T is the temperature, R is the gas constant, L is the total membrane thickness, and F is the Faraday constant.

$$\sigma_{amb} = \frac{\sigma_i \times \sigma_e}{\sigma_i + \sigma_e} \quad (3)$$

The partial conductivity values (σ_i and σ_e) were calculated by combining eqn (1) and (3).

The temperature dependence of conductivity was assessed using activation energy, determined from:

$$\ln(\text{conductivity} \times T) = -\frac{E_a}{R \times T} + k \quad (4)$$

where E_a is the activation energy and k is the rate constant.

Results and discussion

Material characterization

Microstructure and composition. The sintered samples generally exhibit gas-tight microstructures with minimal residual porosity, as evidenced by Fig. 2(a, c and e). Each sample comprises three primary groups of grains, distinguishable by their varied appearances and morphologies. According to previously published findings,[42] concave-shaped grains correspond to newly formed Gd, Fe-rich oxides, while grey and dark grey grains are assigned to a Ce–Gd oxide, and Fe–Co oxides, respectively. The Ce–Gd oxide grains form a continuous matrix that encases the other phases, which are homogeneously distributed as discrete islands, with no observable long-range percolation in the 2D view in Fig. 2.

Further analysis *via* EBSD on randomly selected cross-sections, as shown in Fig. 2(b, d and f), confirms the crystallographic nature of these grains. The grains of the Ce–Gd oxide and the Gd, Fe-rich oxide adopt a $Ce_{1-x}Gd_xO_{2-\delta}$ fluorite and a $GdFeO_3$-type perovskite structure, respectively, while the Fe–Co oxide grains exhibit either a spinel or a rock-salt structure. Notably, the $Ce_{1-x}Gd_xO_{2-\delta}$ fluorite phase, which serves as the ionic conducting phase, constitutes over 80 vol% in every sample due to the 85 wt% $Ce_{0.8}Gd_{0.2}O_{2-\delta}$ precursor input. Whereas, the electronic conducting phases, possessing perovskite, spinel, and rock-salt structure,[28] collectively remain below the theoretical percolation threshold value of 30 vol%.

A comparative assessment reveals that FC-CGO_LT and FC-CGO_HT contain similar proportions of individual electronic conducting phases. However, FCG-CGO_HT exhibits a higher concentration of perovskite and rock-salt phases, coupled with a reduced fraction of the spinel phase. The increased perovskite formation in FCG-CGO_HT suggests an enhanced phase interaction due to the incorporation of Gd_2O_3.

Fig. 3 provides an in-depth illustration of the grain percolation characteristics of ionic and electronic conducting phases, using FC-CGO_HT as an example. As depicted in the right column of Fig. 3(a), nearly all grains of the ionic conducting phase contribute to forming a percolating network. In contrast, as shown in the middle column of Fig. 3(b), the grains of electronic conducting phases fail to form a percolating network due to their insufficient volume. Similar results are observed for FC-CGO_LT and FCG-CGO_HT samples, as shown in Fig. S1(a–d).†

Critical geometry factor for ionic conduction. A mixed conductor composed of both ionic and electronic conducting phases exhibits a lower effective ionic conductivity than a pure ionic conductor, when considering identical macroscopic geometry (characterized by area – S and length/thickness – L). This reduction primarily arises from two factors: (i) volumetric dilution of the ionic conducting phase due to the presence of electronic conducting phases and (ii) increased tortuosity within the ionic conduction network.

The effective geometry factor for ionic conduction is derived from the apparent geometry factor (L/S) through eqn (5),[43,44] which is schematically depicted in the inset of Fig. 4(a).

$$\left(\frac{L}{S}\right)_{effective} = \frac{L}{S} \times \frac{\tau_i}{V_i} = \frac{L}{S} \times N_M \quad (5)$$

where τ_i represents the tortuosity of the ionic conducting network, and V_i denotes the volume fraction of the ionic conducting grains. The τ_i/V_i ratio is known as the so-called MacMullin number (N_M).[43,44] Given that $\tau_i > 1$ and $V_i < 1$ in any

This journal is © The Royal Society of Chemistry 2025

J. Mater. Chem. A, 2025, **13**, 14940–14956 | **14943**

1: Ce$_{1-x}$Gd$_x$O$_{2-\delta}$ fluorite   2: Cobalt iron spinel or rock salt oxide   3: Gd and Fe-rich perovskite oxide
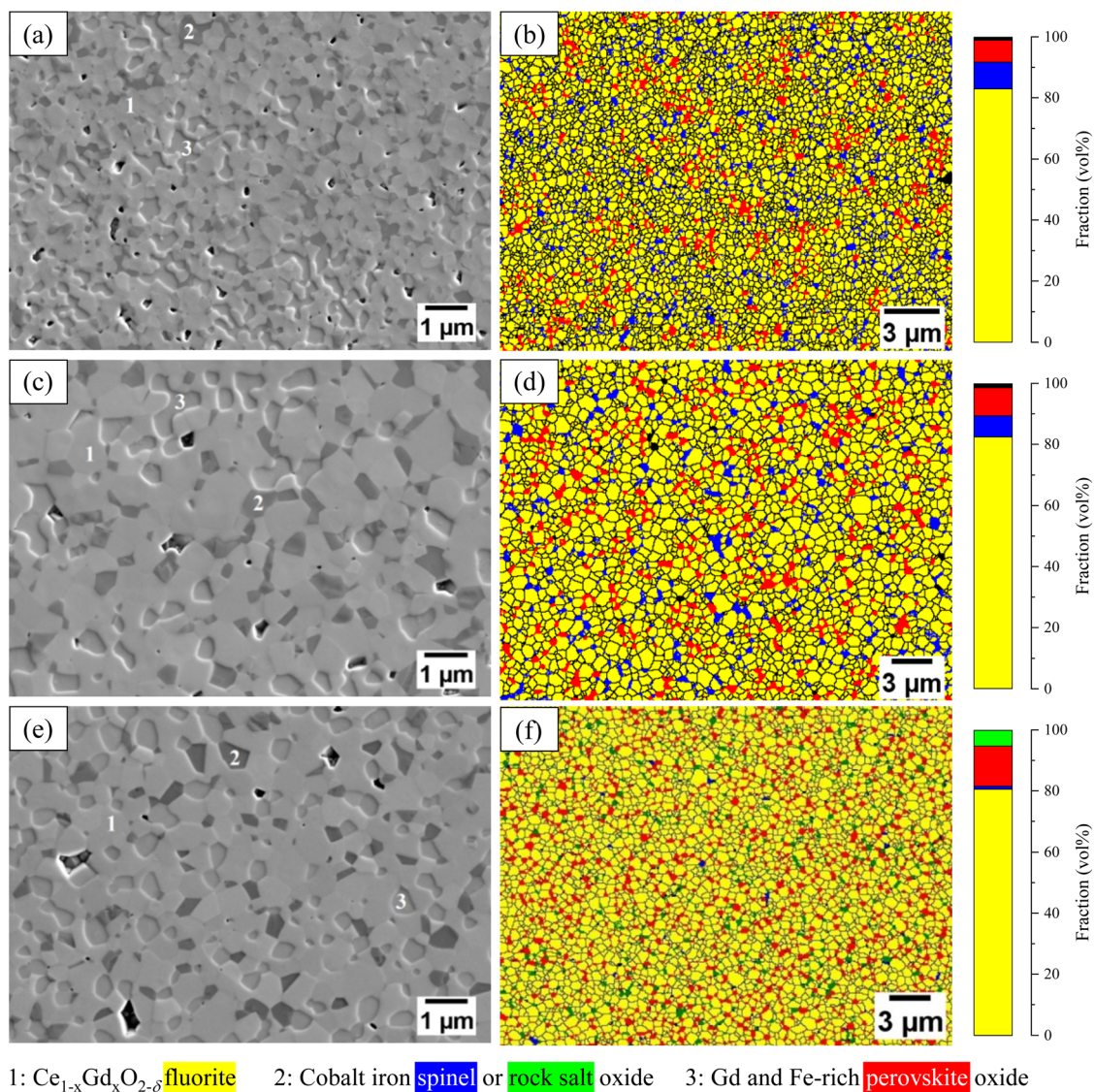
Fig. 2 Microstructural characterization *via* SEM (left column) and EBSD phase mappings (right column) for FC-CGO_LT (a and b), FC-CGO_HT (c and d) and FCG-CGO_HT (e and f). In these images, black dots and lines correspond to pores and grain boundaries, respectively. The annotation given below delineates the specific phases corresponding to the numbered and color-coded grains, with their respective volume fractions provided alongside the individual phase mappings. (a, c and d) were adapted with permission from the previously published studies.[34,36]

composite system, N_M is always greater than 1. Consequently, a low N_M (indicative of a low τ_i and a high V_i) of the ionic conducting phase reflects high ionic conduction efficiency.

The calculated N_M values, presented in Fig. 4(a), follow an increasing trend: FC-CGO_HT < FC-CGO_LT < FCG-CGO_HT. This trend is consistent with the volumetric increase of the ionic blocking but electronic conducting phases, as well as the rise in tortuosity (from 1.503 to 1.566, and to 1.581) of the ionic conducting network. These N_M values are more than one order of magnitude lower than the one (~34.55) calculated for 40CF-CGO_HT, where the high concentration (~41.2 vol%, Fig. S2(a and b)†) of electronic conducting grains leads to severely limited ionic conduction paths with a tortuosity of ~18.44 (Fig. S1(e and f)†).

Critical geometry factor for electronic conduction. For electronic conduction, a distinct geometry factor was applied

because the electronic conducting grains are spatially isolated. Considering electronic conduction between the neighboring electronic conducting grains, the critical geometry factor can be represented by the distances between neighboring electronic conducting grains. These distances were analyzed here *via* the mean linear interception method. Briefly, this method involves 20 randomly placed lines (10 vertical and 10 parallel) onto a binary image containing only the electronic conducting grains, thresholded in black (see Fig. 4(b), inset). Grayscale analysis, performed using ImageJ,[45] yielded intergranular distance distributions. The obtained distribution profiles progressively broaden and shift toward larger distance ranges from FC-CGO_LT to FCG-CGO_HT, and to FC-CGO_HT, as compared in Fig. 4(b). This trend correlates with the observed grain growth in Fig. S3.† Clearly, as grain size increases, electronic conducting grains become more widely spaced, which
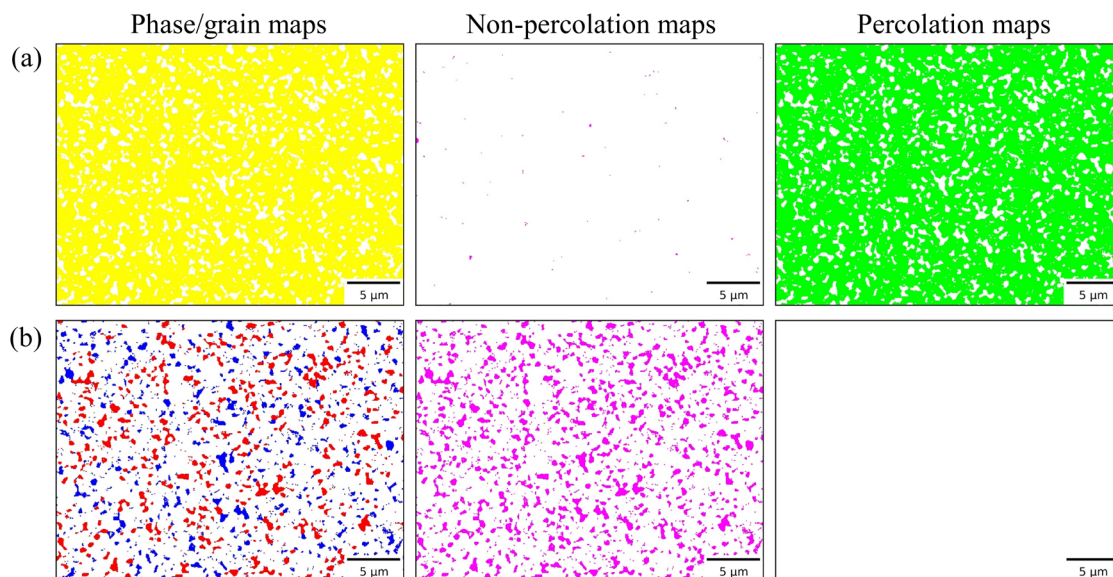
14944 | *J. Mater. Chem. A*, 2025, **13**, 14940–14956

This journal is © The Royal Society of Chemistry 2025

Fig. 3 Overall grain/phase distribution maps (left column), non-percolation maps (middle column) and percolation maps (right column) of ionic conducting phase (a) and electronic conducting phases (b) in FC-CGO_HT.
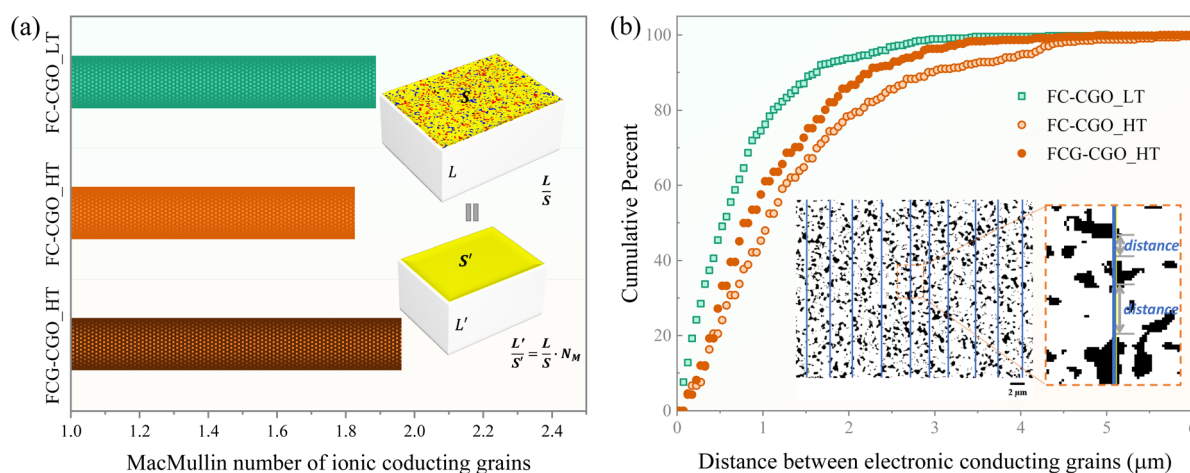

Fig. 4 Critical geometry effects on ionic and electronic conduction reflected by the MacMullin number (ratio of tortuosity to volume fraction) of ionic conducting grains (a) and the intergranular distance distribution profiles for electronic conducting grains (b).

may contribute to an increase in electronic conduction resistance.

Grain boundary investigation. Fig. 5 illustrates that the grain boundaries of the ionic conducting phase, *i.e.*, the $Ce_{1-x}Gd_x$-$O_{2-\delta}$ fluorite, exhibit Ce depletion alongside Gd, Fe, and Co enrichment. The observed Ce depletion and Gd segregation are well-documented phenomena in sintered $Ce_{1-x}Gd_xO_{2-\delta}$ fluorite compounds without any additives.[46–48] Uniquely, the investigation of FC-CGO_HT in Fig. 5(b) reveals the presence of two parallel Gd segregation lines near the grain edges, despite the limited resolution.

Based on the EDXS elemental mapping, the cation intensity ratios (Gd/Ce, Fe/Ce, and Co/Ce) are detailed in Fig. 6. The Gd/Ce ratio exhibits a greater increase from the grain interior to the boundary in FC-CGO_HT than in FC-CGO_LT, suggesting that

Gd segregation is enhanced at higher sintering temperatures. Additionally, in FC-CGO_HT, the Gd/Ce ratio exhibits a relaxation at the grain boundary core, with its maximum values occurring at positions adjacent to the core. This observation corroborates previous atomic-scale investigations, which revealed ordered Gd segregation at two atomic planes adjacent to the core.[33,35] Analogous phenomena have been reported in Y-stabilized zirconia, where ordered Y segregation at grain boundary vicinities has been observed experimentally and simulated computationally.[49]

In contrast, the Fe/Ce and Co/Ce ratios show a considerably weaker increase from the grain interior to the boundary in FC-CGO_HT than in FC-CGO_LT, suggesting that a higher sintering temperature inhibits Fe and Co segregation. This trend aligns with prior studies on Co-modified $Ce_{0.8}Gd_{0.2}O_{2-\delta}$[50,51] and

This journal is © The Royal Society of Chemistry 2025

J. Mater. Chem. A, 2025, **13**, 14940–14956 | **14945**
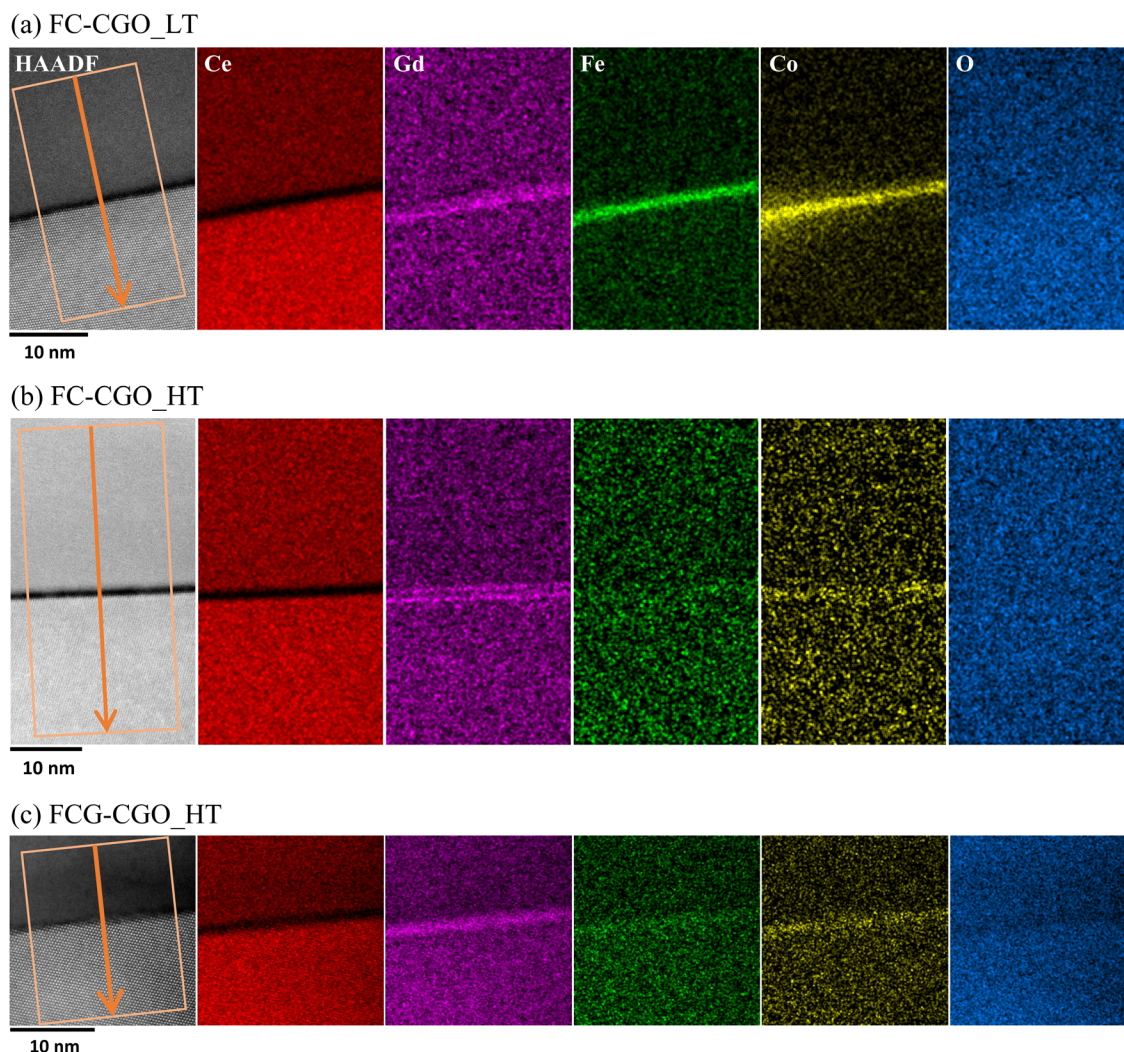
(a) FC-CGO_LT

(b) FC-CGO_HT

(c) FCG-CGO_HT

Fig. 5 Elemental mapping *via* EDXS across ceria grain boundaries in FC-CGO_LT (a), FC-CGO_HT (b), and FCG-CGO_HT (c). The upper grain is randomly oriented, while the lower one is along its [101] zone axis.

$Ce_{0.8}Tb_{0.2}O_{2-\delta}$,[20] which indicates that significant Co enrichment at ceria grain boundaries is only feasible below ∼1100 °C.

Following the incorporation of Gd_2O_3, FCG-CGO_HT exhibits the smallest increase in all cation intensity ratios from the grain interior to the boundary. In some cases, ceria grain boundaries appear nearly devoid of Fe and Co segregation (see Fig. S4†). This suggests that Gd_2O_3 acts as a grain boundary scavenger.

In-depth analysis across ceria grain boundary in FC-CGO_LT. Due to the pronounced overall grain boundary segregation, FC-CGO_LT was investigated in more detail *via* high-resolution (atomic level) EELS. Fig. 7(a) presents an annular dark-field (ADF) image, where bright spots correspond to cation positions. The grain boundary exhibits a well-crystallized structure, indicating the absence of significant amorphous phases or interstitial cations. Elemental intensity maps for Ce $M_{4,5}$, Gd $M_{4,5}$, Fe $L_{2,3}$, Co $L_{2,3}$ and O K edges (Fig. 7(b)) reveal that cation distributions closely resemble those in Fig. 5(a). Notably, grain boundary atomic positions are predominantly occupied by Gd, while Fe and Co positions remain unresolved due to diffuse intensity patterns. Around the atomic positions most enriched in Gd (indicated by the gray arrows in Fig. 7(b)), a noticeable reduction in O intensity is observed. This observation suggests the co-segregation of Gd'_{Ce} with $V_O^{\bullet\bullet}$, leading to the formation of dopant–vacancy complexes.

The oxidation state of Ce was determined using Ce $M_{4,5}$-edge EELS spectra. As shown in Fig. 7(c), the spectra feature two characteristic peaks – Ce M_4 and M_5. The overall peak intensities are weaker at the grain boundary core (C) than in the grain bulk regions (R and L), reflecting either a lower Ce density or a reduced grain boundary thickness. A noticeable increase in the M_5/M_4 intensity ratio is observed at the grain boundary core compared to the grain interior, indicative of a partial reduction of Ce^{4+} to Ce^{3+}.[33,35,46,52,53] The Ce^{3+} fraction (x) was quantified using the relationship $R = 0.925(1 - x) + 1.25x$,[33] where R is the M_5/M_4 intensity ratio in second derivative spectra and 0.925 and 1.25 represent reference R values for Ce^{4+} and Ce^{3+},

14946 | *J. Mater. Chem. A*, 2025, **13**, 14940–14956

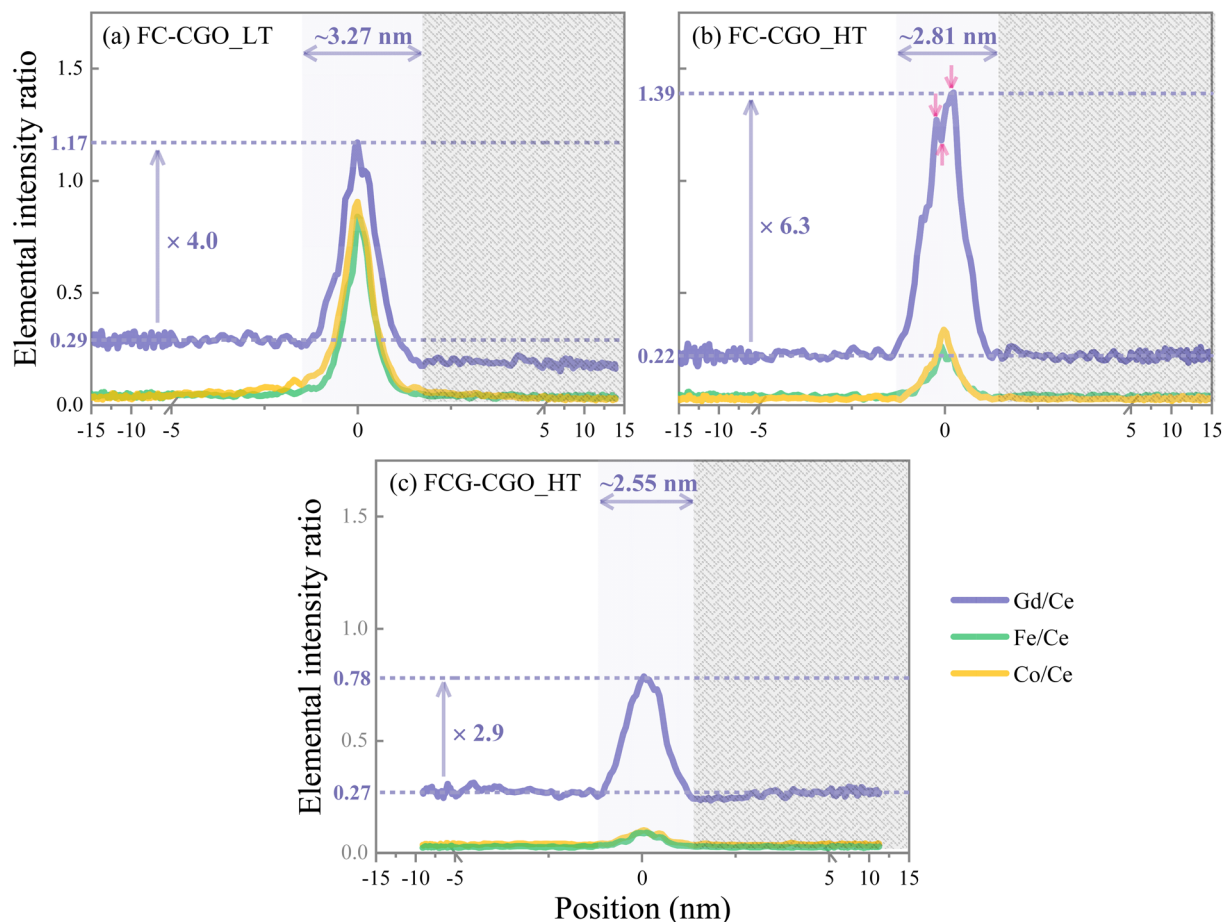This journal is © The Royal Society of Chemistry 2025

Fig. 6 Elemental intensity ratios across ceria grain boundaries in FC-CGO_LT (a), FC-CGO_HT (b), and FCG-CGO_HT (c). The left grain is randomly oriented, while the right one is along its [101] zone axis. The EDXS scanned areas and directions are indicated in the HAADF images obtained by STEM as shown in the first column of Fig. 5.

respectively.[54] The highest R value of 1.137, determined near the grain boundary core, corresponds to a Ce^{3+} fraction of ~65.2%, as shown in Fig. 7(d). This R value falls within the range reported for $Ce_{0.85}Gd_{0.11}Pr_{0.04}O_{2-\delta}$ ($R = 1.0$)[55] and $Ce_{0.8}Gd_{0.2}O_{2-\delta}$ ($R = 1.2$),[47] confirming a reasonable estimation.

Unlike Ce, Fe cations at ceria grain boundaries are predominately stabilized as Fe^{3+}, as reported in previous studies.[33,56] In contrast, the oxidation states of Co can vary among 2+ and 3+, as evidenced by the coexistence of spinel and rock-salt phases. However, precise determination of Co oxidation states remains challenging due to excessive noise in its $L_{2,3}$ spectra (not shown here).

Grain boundary charge state analysis. According to classical space charge theory for acceptor-doped ceria and zirconia,[57] oxygen vacancies ($V_O^{\bullet\bullet}$) exhibit an enhanced concentration at grain boundary cores. This localized enrichment generates positively charged cores that repel positive charge carriers ($V_O^{\bullet\bullet}$ and electronic holes) while attracting negatively charged ones (electrons and acceptor dopants like Gd_{Ce}'). This redistribution of charge carriers leads to the formation of space charge layers in the vicinity of the core region, which contributes to partially or fully neutralizing the space charge potential.

However, for FC-CGO_LT, the O intensity monotonously decreases from the ceria grain interior to the ceria grain boundary (see Fig. 7(d)), with no evident O-enriched or $V_O^{\bullet\bullet}$ depleted region adjacent to the grain boundary core. This observation aligns with previous studies on ceria and zirconia that reported O depletion peaks at grain boundary cores without evidence of adjacent O-enriched or $V_O^{\bullet\bullet}$ depleted layers,[47,58–60] suggesting that directly picturing oxygen vacancy profiles remains challenging. An additional analysis of cations' valence states and occupation sites is therefore conducted.

The presence of Ce^{3+} at the grain boundary indicates the absence of bounded oxygen, which is consistent with the observed decrease in O intensity (Fig. 7(d)). Since only ~0.8% of CeO_2 can be thermally reduced to Ce_2O_3 even at 1420 °C,[61] and considering FC-CGO_LT's low sintering temperature (1050 °C), the observed high Ce^{3+} fractions cannot be attributed to thermal reduction. Instead, it likely arises from the grain boundary structure, where $V_O^{\bullet\bullet}$ formation and accumulation are energetically favorable or structurally necessary.[52,53]

The absence of interstitial cations in Fig. 7(a) suggests Fe and Co primarily substitute the Ce sites, though their precise atomic positions remain unresolved. Thus, the Fe and Co cations (average valence < 4+) appear to act as heterogeneous
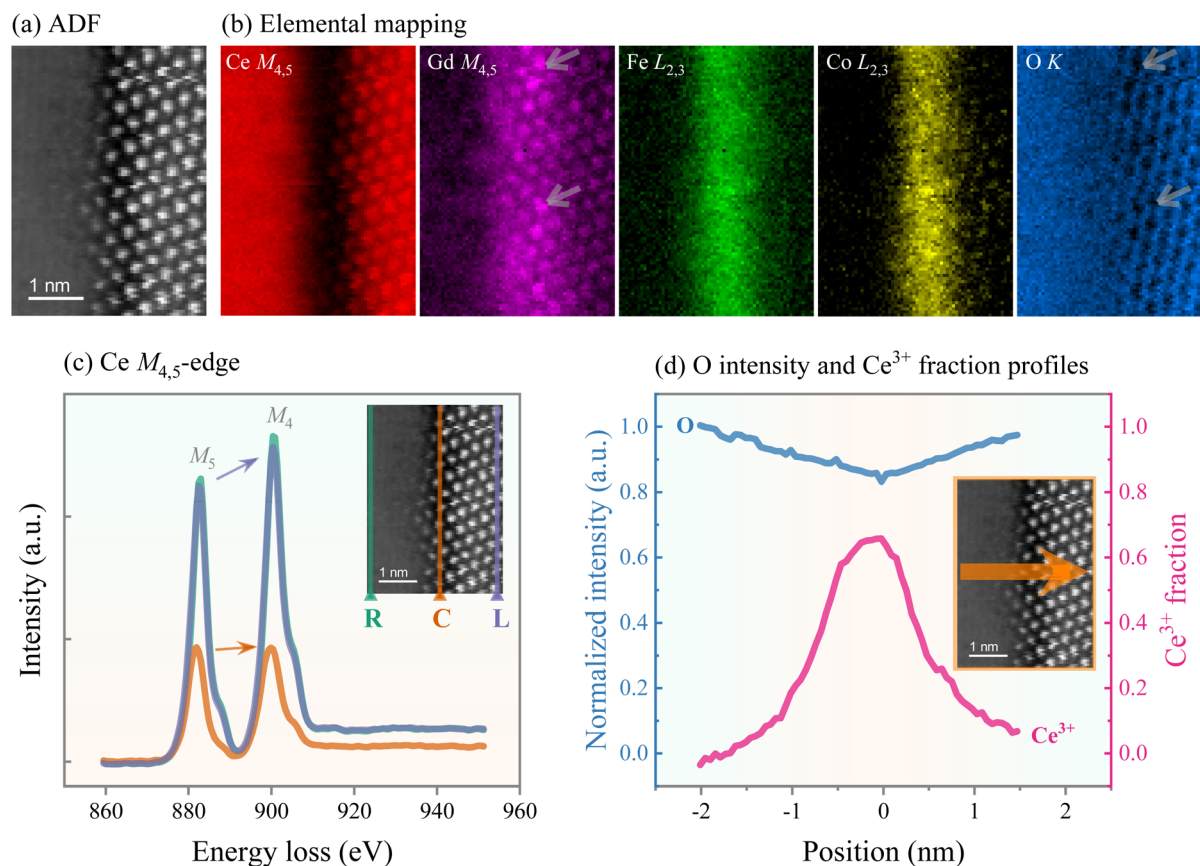
Fig. 7 STEM-EELS analysis across the ceria grain boundary in FC–CGO_LT: (a) the simultaneously recorded ADF (annular dark field) image; (b) elemental intensity maps from Ce $M_{4,5}$, Gd $M_{4,5}$, Fe $L_{2,3}$, Co $L_{2,3}$ and O K edges based on EELS spectrum imaging; (c) representative Ce $M_{4,5}$-edge EELS spectra collected from different positions, including the grain boundary core (C) and the adjacent grain interior regions (R and L) as indicated in the inset ADF image; (d) The O intensity and the calculated Ce^{3+} fraction profiles across the region shown in the inset. The left grain is randomly oriented, while the right one is along its [101] zone axis.

acceptor dopants localized almost exclusively at ceria grain boundaries. They diffuse externally from the additive sources rather than internally from the ceria grain bulk.

Given the high concentrations of Fe'_{Ce}, Co'_{Ce}, Co''_{Ce} and Gd'_{Ce} for charge compensation, it is surprising that there is still an excess of oxygen vacancies, necessitating Ce^{4+} reduction. We believe that the high Ce^{3+} faction is associated with the emergence of a grain boundary superstructure,[62] which possesses a lower oxygen coordination as compared to the CeO_2 fluorite structure. Consequently, the investigated ceria grain boundary is not expected to exhibit substantial charge imbalance.

This analysis does not provide evidence for the formation of space charge layers for FC-CGO_LT. Instead, it reveals a co-enrichment of acceptors and $V_O^{••}$ at the grain boundary, closely resembling the behavior observed in doped ceria with a high acceptor concentration at grain boundaries.[63]

With increased sintering temperature for FC-CGO_HT and FCG-CGO_HT, the situation may change and will be discussed later.

Mechanisms of grain boundary composition evolution. The observed grain boundary compositions can be rationalized by considering temperature-dependent diffusion and segregation pathways of transition elements. These elements may: (1)

diffuse to ceria particle surfaces, (2) segregate at ceria grain boundaries, (3) dissolve into ceria lattices, forming a solid solution, or (4) precipitate as a secondary phase.

At relatively lower temperatures (800–900 °C), transition metal cations preferentially accumulate at ceria particle surfaces and grain boundaries,[50,51,64] which is driven by energy minimization mechanisms and promotes densification of ceria particles.[65] As temperature increases, the closure of free surfaces and grain boundary coalescence lead to the over-saturation of cation segregation, ultimately triggering the precipitation of secondary phases. The observed Fe and Co segregation profiles for FC-CGO_LT and FC-CGO_HT align well with this framework.

For FCG-CGO_HT, minimal Fe and Co segregation supports the hypothesis that Gd_2O_3 scavenges Fe and Co segregation. This phenomenon is attributed to the formation of a $Gd_{1-x}Ce_xFe_{1-y}Co_yO_{3-\delta}$ perovskite phase at temperatures above 1050 °C.[36] Consequently, Fe and Co cations, which segregate at low temperatures, are effectively removed upon the formation of this perovskite phase. The reduction in Fe and Co segregation also leads to a decrease in grain boundary mobility at the higher temperature of 1200 °C, as evidenced by the

14948 | *J. Mater. Chem. A*, 2025, **13**, 14940–14956

This journal is © The Royal Society of Chemistry 2025

smaller grain size of FCG-CGO_HT relative to FC-CGO_HT (see Fig. S3†).

Regarding Gd segregation, its driving force can be partially attributed to grain boundary energy reduction,[63] although the prevailing explanation involves the space charge effect.[57,66,67] The contribution of lattice strain relaxation is considered minimal due to the relatively small ionic radius mismatch between Gd and Ce.[57,66]

As analyzed previously for FC-CGO_LT, the space charge effect is not evident. The relatively low sintering temperature (1050 °C) is likely to result in either incomplete formation or inhibition of space charge layers due to the early-stage accumulation of Fe and Co acceptors alongside $V_O^{\cdot\cdot}$. Besides, once the grain boundary is decorated with Fe and Co cations, the overall boundary energy is expected to decrease, facilitating the segregation of Gd from the grain interior, where it exists at a higher energy state.

As the sintering temperature increases in FC-CGO_HT, it remains uncertain whether the enhanced Gd segregation arises from an emerging space charge effect or is a consequence of grain boundary migration and merging.

For FCG-CGO_HT, the observed minimal Gd segregation may be attributed to inhibited grain boundary migration and/or moderate grain boundary energy reduction, achieved by removing Fe and Co while simultaneously introducing Gd through the Gd_2O_3 additive. Additionally, the Gd_2O_3 additive may further suppress space charge layer formation by neutralizing excess core charge through Gd doping directly at the grain boundary.[68] This hypothesis is well supported by a low fraction of Ce^{3+} (~48.5%, see Fig. S5†), implying less excess of $V_O^{\cdot\cdot}$.

Nevertheless, variations among grain boundaries remain, necessitating the following macroscopic assessments.

Material assessments

Total conductivity in respective atmospheres. Total conductivity measurements were performed under air and Ar, respectively, as a function of temperature. The obtained Cole–Cole plots of impedance data were analyzed following the procedure described in ESI Note 2.† Since it is not possible to separate grain interior and boundary contributions, only total resistances/conductivities are derived.

Under air conduction, see Fig. 8(a), the highest and lowest σ_{tot} were measured for the EC and IC samples, respectively. The σ_{tot} values of the IC sample closely match those of a reference single-phase fluorite compound $Ce_{0.9}Gd_{0.1}O_{2-\delta}$ (densified at 1300 °C for 3 h in air using powders produced by Solvay). This similarity suggests that the IC sample consists of a fluorite phase with a Ce : Gd ratio of approximately 9 : 1 (rather than the initial 8 : 2 ratio), while the influence of secondary phases (~4.5 vol% as given in Fig. S2(c and d)†) is negligible.

The σ_{tot} values of the mixed conductors fall between those of the EC and IC samples, following the trend: FC-CGO_LT > FCG-CGO_HT > FC-CGO_HT. Notably, FC-CGO_LT exhibits superior σ_{tot} above 800 °C, outperforming other mixed conductors with comparable content (≤20 vol% or 15 wt%) of electronic conducting phase,[69–71] as compared in Fig. 8(b).

Under Ar conduction, as shown in Fig. 8(c), the EC sample retains the highest σ_{tot}, whereas FC-CGO_HT exhibits the lowest. The σ_{tot} of FC-CGO_LT and FCG-CGO_HT are comparable to that of the IC sample, indicating a significantly increased contribution from the ionic conductivity, accompanied by a decrease in the electronic conductivity.

A comparison of the percentage change in σ_{tot} values from air to Ar (Fig. S6†) reveal that the IC sample experiences a marginal fluctuation in total conductivity, consistent with its dominant ionic conduction mechanism controlled by the fluorite phase. In contrast, the EC sample and all mixed conductors are subject to a reduction in σ_{tot} from air to Ar, indicative of a p-type (hole) conduction mechanism. This reduction is substantially greater for the mixed conductors than for the EC sample, suggesting divergent p-type conduction mechanisms between these two systems. These differences may arise from variations in polaronic defect structures and disparate hopping pathways.

The temperature-dependence conductivity was further analyzed through activation energy, as present in Fig. 8(e). All samples exhibit positive activation energies, confirming a semiconductor-like behavior where conductivity increases with rising temperature.

Under air conditions, a clear distinction in activation energies is observed among the samples, with the IC sample displaying the lowest and FC-CGO_LT the highest.

Under Ar conditions, the activation energies of mixed conductors become comparable to that of the IC sample, indicating a rising contribution from ionic conduction.

For the IC sample, the activation energy remains similar to that of the $Ce_{0.9}Gd_{0.1}O_{2-\delta}$ regardless of the atmosphere, reaffirming its pure ionic conduction behavior. However, for the other samples, activation energy decreases when transitioning from air to Ar, with the reduction being more pronounced in mixed conductors than in the EC sample. For instance, FC-CGO_LT exhibits a remarkable 46% decrease in activation energy.

This comprehensive comparison confirms that the mixed conductors indeed exhibit mixed ionic and p-type conductivity. The ionic conductivity is attributed to the fluorite phase, while the p-type conductivity is unlikely to be dominated by the electronic conducting phases. Instead, alternative pathways through the grain boundaries of the ionic conducting phase are likely controlling the overall electronic conduction.

Similar to Pr-doped ceria,[72] a small polaron hopping mechanism is proposed to explain the observed electronic conduction along ceria grain boundaries. The conductivity suppression under Ar conditions is attributed to the reduction of Co cations. In other words, a more uniform distribution of Co valence states leads to a reduction of polaronic defect concentrations.

Total conductivity under an Ar-to-air gradient. Given the substantial influence of atmospheric conditions on conductivity, it is essential to evaluate the *operando* conducting behavior of the mixed conductor under dual-atmosphere applications. One such scenario is oxygen permeation, where Ar and air are applied separately to opposite sides of the mixed conductor. In this case, the conductivity is not spatially uniform but varies continuously across the sample thickness.

This journal is © The Royal Society of Chemistry 2025

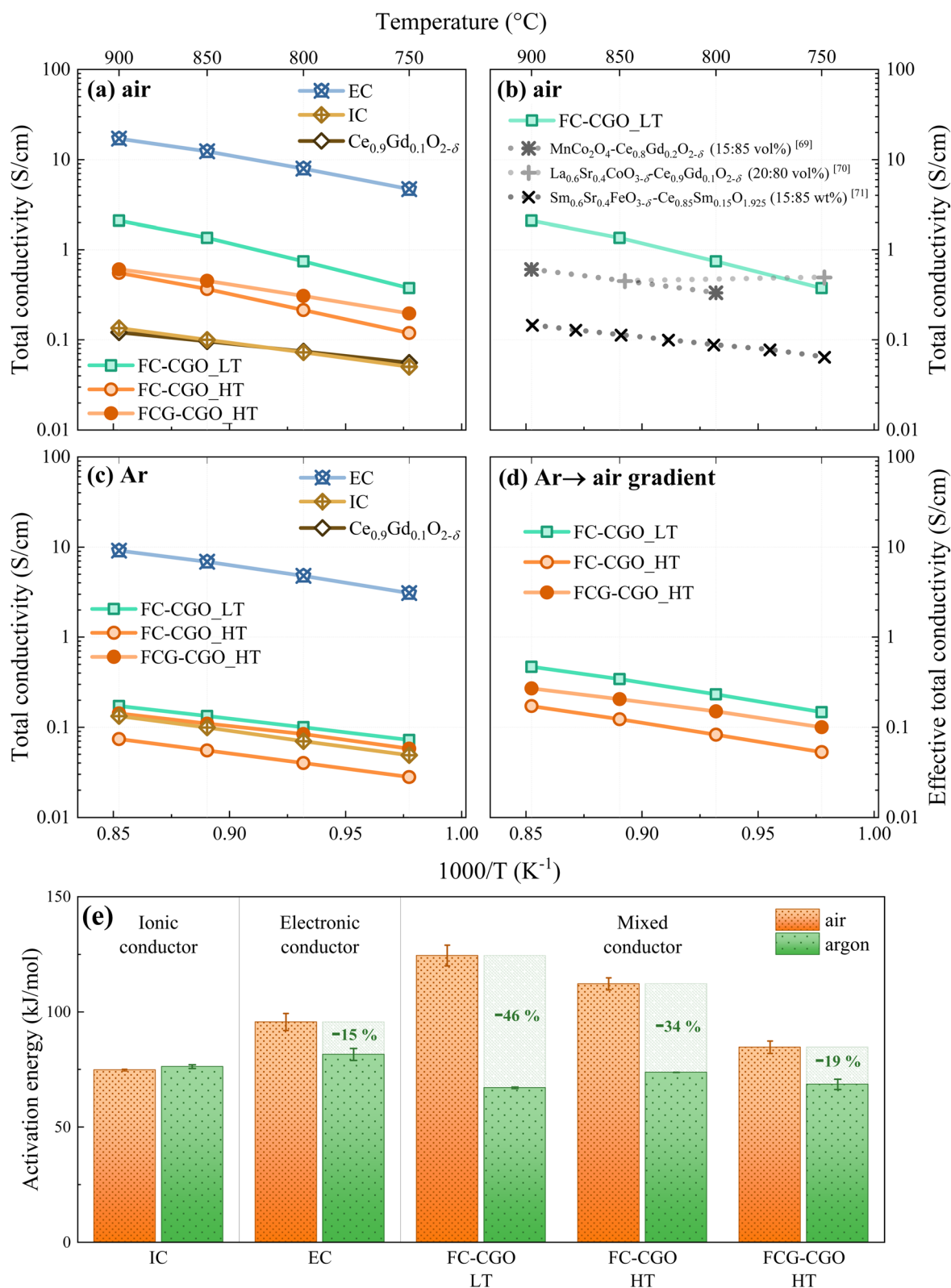*J. Mater. Chem. A*, 2025, **13**, 14940–14956 | **14949**

Fig. 8 Total conductivity measured in air (a), Ar (c), and Ar-to-air gradient (d) with the corresponding activation energies given in (e). In (b), several conductivity values in air reported for mixed conductors having a comparable content (≤20 vol% or 15 wt%) of electronic conducting phase are shown for comparison.[69–71]

14950 | J. Mater. Chem. A, 2025, 13, 14940–14956

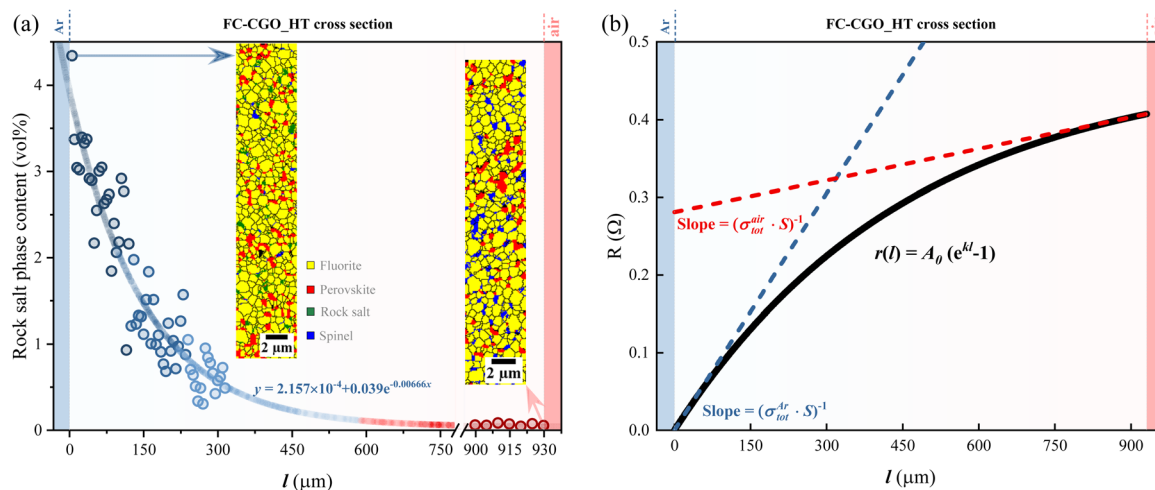This journal is © The Royal Society of Chemistry 2025

Fig. 9 Gradient variation of the rock-salt phase content (a) and total resistance (b) across the thickness of FC-CGO_HT after the oxygen permeation test, where the two sample surfaces were exposed to Ar and air, respectively, below ~1020 °C. The rock-salt phase content was quantified from EBSD data with a step width of 5 μm, and fitted using a natural exponential function. The total resistance was calculated assuming a natural exponential decay behavior.

Consequently, resistance does not exhibit a linear dependence on thickness.

We adopt the rock-salt phase as a tracer for the impact of Ar, and investigate FC-CGO_HT using EBSD at the cross-section after the oxygen permeation measurement. As shown by the phase mappings in Fig. 9(a), a notable variation in the rock-salt phase is observed, with negligible content on the air side but a substantial increase on the Ar side. The spatial distribution of the rock-salt phase across the sample thickness follows a natural exponential decay.

It is assumed that resistance growth with sample thickness also follows a natural exponential function, mathematically expressed as eqn (6) and plotted in Fig. 9(b).

$$r(l) = A_0(e^{kl} - 1) \tag{6}$$

where $r(l)$ represents the resistance function against sample thickness (l), which passes through the coordinate's origin ($r(0) = 0$). And A_0 and k are constants.

At $l = L$ (total sample thickness), the total effective resistance under an Ar-to-air gradient, denoted as R_{tot}^{eff}, is obtained. This value determines the effective total conductivity ($\sigma_{tot}^{eff}|_{Ar \to air}$) via:

$$\sigma_{tot}^{eff}|_{Ar \to air} = \frac{L}{S} \times \frac{1}{R_{tot}^{eff}} = \frac{L}{S} \times \frac{1}{r(l)|_{l=L}} \tag{7}$$

At the sample surface, the slope of $r(l)$ corresponds to the total conductivity in Ar (σ_{tot}^{Ar}) or air (σ_{tot}^{air}), as expressed by eqn (8) and (9) (also plotted as the dashed lines in Fig. 9(b)).

$$\frac{dr}{dl}\Big|_{l=0} = \frac{1}{\sigma_{tot}^{Ar} \times S} \tag{8}$$

$$\frac{dr}{dl}\Big|_{l=L} = \frac{1}{\sigma_{tot}^{air} \times S} \tag{9}$$

By combining eqn (6)–(9), the $\sigma_{tot}^{eff}|_{Ar \to air}$ can be derived as:

$$\frac{\sigma_{tot}^{eff}|_{Ar \to air}}{\sigma_{tot}^{Ar}} = \frac{\ln \gamma}{\gamma - 1} \tag{10}$$

where γ is defined as the ratio of total conductivity in Ar to that in air:

$$\gamma = \frac{\sigma_{tot}^{Ar}}{\sigma_{tot}^{air}} \tag{11}$$

A key advantage of this formulation is that it eliminates all constants associated with the assumed natural exponential function, allowing $\sigma_{tot}^{eff}|_{Ar \to air}$ to be determined solely based on separately measured total conductivities in air and Ar. This approach can be extended to other materials, provided that $r(l)$ follows an exponential dependence with only two independent constants.

As shown in Fig. 8(d), the calculated $\sigma_{tot}^{eff}|_{Ar \to air}$ deviates from σ_{tot}^{air} but converges towards σ_{tot}^{Ar}. This trend underscores the dominant influence of the lower oxygen partial pressure on total conductivity. The dominating portion (either ionic or electronic conductivity) of $\sigma_{tot}^{eff}|_{Ar \to air}$ will be discussed later.

Oxygen permeation. All the measured samples are oxygen permeable, confirming their mixed ionic and electronic conducting nature. The oxygen permeance values for membranes with a thickness of approximately 1 mm are compared in Fig. 10, following the order: FC-CGO_LT ≈ FCG-CGO_HT > FC-CGO_HT. This trend suggests that high-temperature sintering with extended hold time has a detrimental effect on oxygen permeation, whereas the addition of Gd_2O_3 exerts a beneficial influence.

Notably, substantially lower oxygen permeances have been reported for a similar mixed conductor prepared from 80 vol% $Ce_{0.8}Gd_{0.2}O_{2-\delta}$ (nano-sized powder) and 20 vol% $CoFe_2O_4$ (in a preformed state rather than a raw Fe_2O_3 and Co_3O_4 mixture used here).[27] This reference sample (denoted as CF-CGO_ref.) is included in Fig. 10 for comparison. The additive's initial state
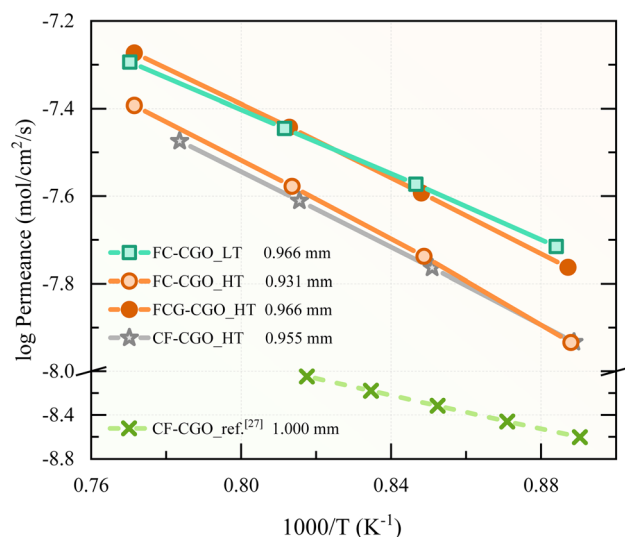
Fig. 10 Oxygen permeances of membranes with thicknesses close to 1 mm.

(preformed spinel or raw oxide mixture) is expected to have limited influence on oxygen permeation, since the spinel phase inherently forms at ~900 °C.[36] However, the additive's Fe : Co ratio (either 1 : 2 or 2 : 1) may play a role.

To further investigate this, FC-CGO_HT precursors were modified by increasing the $Fe_2O_3 : Co_3O_4$ molar ratio from 3 : 4 to 3 : 1, yielding $CoFe_2O_4$. Other preparation steps remained unchanged, producing the CF-CGO_HT sample. Its oxygen permeances are comparable to those of FC-CGO_HT but higher than the ones of CF-CGO_ref.,[27] indicating that the Fe : Co ratio (1 : 2 vs. 2 : 1) has a negligible effect on oxygen permeation.

Another potential factor influencing oxygen permeation is the initial particle size of $Ce_{0.8}Gd_{0.2}O_{2-\delta}$ powder, which will be discussed later.

Ambipolar conductivity. The measured oxygen permeation data were used to determine σ_{amb} via eqn (2), assuming negligible surface exchange effects. As shown in Fig. S7,† the oxygen permeance for both FC-CGO_LT and FC-CGO_HT as a function of membrane thickness can be well-fitted to eqn (2) across all temperatures, confirming the validity of eqn (2) for membrane thicknesses exceeding 0.3 mm.

The calculated ambipolar conductivities, see Fig. 11(a), show variations among samples that mirror the trends observed in oxygen permeances. The derived activation energy values closely match previously reported values for the ionic conductivity of pure Gd-doped ceria,[27,29,30,73] but are significantly lower than those of CF-CGO_ref.[27] This indicates that σ_{amb} of the mixed conductors synthesized here is predominantly governed by the ionic conductivity. In contrast, for CF-CGO_ref.,[27] σ_{amb} is likely limited by the electronic conductivity, being associated with the depletion of Fe and Co grain boundary segregation.[27]

By combining the σ_{amb} with the previously determined $\sigma_{tot}^{eff}|_{Ar/air}$, the effective partial conductivities under an Ar-to-air gradient were resolved and are compared in Fig. 11(b). The results demonstrate that the effective electronic conductivities substantially exceed the effective ionic conductivities, confirming that ionic transport is the limiting factor for σ_{amb}.

Electronic conductivity. The effective electronic conductivity follows the trend: FC-CGO_LT > FCG-CGO_HT > FC-CGO_HT.

The highest effective electronic conductivity values observed for FC-CGO_LT can be attributed to: (1) the highest concentration of Fe and Co cations at ceria grain boundaries (see Fig. 6), where Co cations can exist in mixed valence states; (2) the shortest transport paths along ceria grain boundaries, represented by the shortest distance between electronic conducting grains, as indicated in Fig. 4(b).

The lowest effective electronic conductivity for FC-CGO_LT is then explained by the reduced Fe and Co segregation and extended transport paths.
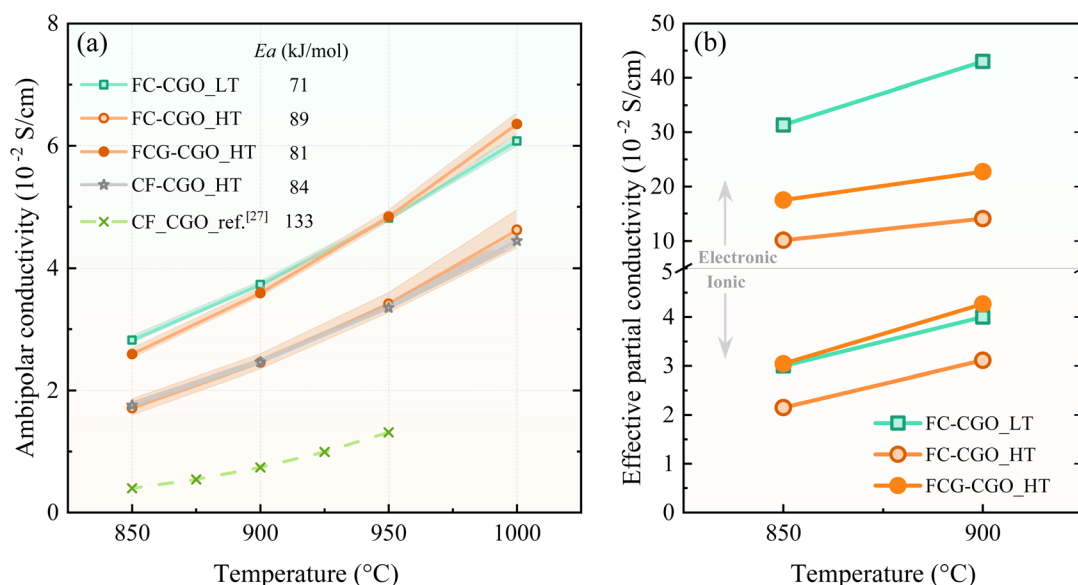

Fig. 11 Ambipolar conductivity (a) derived from oxygen permeation and effective partial conductivities (b) calculated from ambipolar conductivity and effective total conductivity.

14952 | J. Mater. Chem. A, 2025, **13**, 14940–14956

This journal is © The Royal Society of Chemistry 2025

However, this interpretation does not fully account for the moderate electronic conductivity observed for FCG-CGO_HT, where Fe and Co segregation at grain boundaries is nearly absent. This discrepancy suggests an alternative conduction mechanism, such as Fe and Co cations dissolving into the ceria lattice rather than forming grain boundary decorations. Further confirmation was obtained by examining a sample subjected to a 1 minute dwell time at 1200 °C, followed by rapid air quenching. Elemental mappings across the grain boundary (Fig. S8†) revealed Co enrichment in the grain interior near the boundary, representing an initial stage of Co diffusion into the ceria lattice. This diffusion is unlikely for FC-CGO_LT and FC-CGO_HT because: (1) for FC-CGO_LT, the lower sintering temperature (1050 °C) restricts Co incorporation into the lattice; (2) for FC-CGO_HT, the nearly ordered Gd segregation at the grain boundary can inhibit Co diffusion into ceria lattice.

Based on these findings, a distinct electronic conduction mechanism is proposed for FCG-CGO_HT: electronic transport is facilitated by Co-doped ceria grains rather than ceria grain boundary decorations. This accounts for the lowest activation energy of total conductivity (dominated by electronic conductivity) in air, as shown in Fig. 8(e).

Ionic conductivity. The effective ionic conductivity follows the order: FCG-CGO_HT ≥ FC-CGO_LT > FC-CGO_HT.

Despite the most favorable and lowest N_M (see Fig. 4(a)), FC-CGO_HT shows the lowest effective ionic conductivity, which correlates with the presence of strongly ordered Gd segregation (Fig. 5(b) and 6(b)) or a high space charge potential at ceria grain boundaries. Whereas, the partially ordered segregation (Fig. 7(b)) in FC-CGO_LT results in higher effective ionic conductivity.

In FCG-CGO_HT, the reduction in grain boundary core charge due to Gd doping may enhance ionic conduction across the grain boundary.[68] Additionally, Co lattice doping increases oxygen vacancy concentrations, further contributing to enhancing lattice ionic conductivity.

Stability. To evaluate long-term reliability, FC-CGO_LT was operated under the permeation conditions for approximately 10 days at 857 ± 1 °C. During this period, gas analysis was interrupted once for mass spectrometer recalibration.

As presented in Fig. 12, both oxygen permeance and ambipolar conductivity experience minor fluctuations of ±2–3% without a discernible time-dependent trend. This observation confirms that FC-CGO_LT sustains a steady high-performance state, attributed to the robustness of its mixed ionic and electronic conducting structure. Moreover, effects from a potential elemental diffusion under an oxygen partial pressure gradient are not reflected and might be excluded in this case.

Further remarks. The primary advantage of FC-CGO_LT is its high electronic conductivity, attributed to the Fe- and Co-cation decoration at ceria grain boundaries. The Co cations in mixed valence states play a more critical role. Notably, achieving such decoration does not require a specific Fe : Co ratio in the additives. We propose that even pure Co_3O_4 additives could yield comparable performance. However, attempts to prepare pure Co_3O_4-modified $Ce_{0.8}Gd_{0.2}O_{2-\delta}$ were unsuccessful, as samples cracked into pieces after sintering due to thermal mismatch. This suggests that a certain Fe_2O_3 content is necessary in combination with Co_3O_4 to improve thermal compatibility with ceria.

Interestingly, Y-stabilized ZrO_2 appears to be mechanically compatible with Co_3O_4. A study by B. Aktas et al.,[74] successfully prepared 8 mol% Y-stabilized ZrO_2 with up to 15 wt% Co_3O_4 without cracking. Their findings also noted a slight increase in grain boundary conductivity, though significantly lower than in the present work. To achieve comparable conductivity levels, the high sintering temperature (1400 °C) used in their study should be reduced to prevent Co precipitation from zirconia grain boundaries.

Other transition metal elements, such as Cr, Mn, Ni, and Cu, exhibit high solubility and diffusivity at ceria grain boundaries as well.[75] These elements show variable valences upon heating or under different atmospheres, and they are expected to have a similar electronic impact on ceria grain boundaries if low-temperature densification is achieved. However, their effects on ionic conductivity differ. Unlike Fe, Co, Ni, and Cu, elements like Cr and Mn possess valence states higher than 4+. They act as donors with no contribution to balancing excess core charge. As a result, they are not beneficial for ionic conduction.[31,76–78]

It is noteworthy that transition metal elements leaching from perovskites, such as $La_{0.6}Sr_{0.4}CoO_{3-\delta}$[70] and $Sr_{0.4}Sm_{0.6}FeO_{3-\delta}$,[71] result in lower conductivity compared to Fe–Co spinel oxides, as shown in Fig. 8(b). This is likely due to: (1) stabilization of Fe and Co cations within the perovskite lattice, preventing them from diffusing to ceria grain boundaries; (2) interdiffusion of more cations between perovskites and ceria,[79,80] which can reduce oxygen permeation as reported in multiple studies.[81–83]

Besides, the grain boundary decoration of transition metal elements is also influenced by the initial surface area of ceria particles. Notably, nanosized $Ce_{0.9}Gd_{0.1}O_{2-\delta}$ exhibits no sintering enhancement upon cobalt oxide addition,[84] suggesting

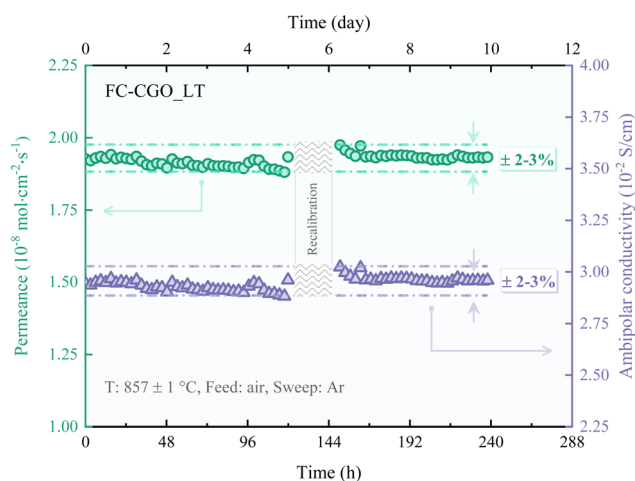**Fig. 12** Time dependence of oxygen permeance and ambipolar conductivity of FC-CGO_LT.

This journal is © The Royal Society of Chemistry 2025

J. Mater. Chem. A, 2025, **13**, 14940–14956 | **14953**

that only limited Co coverage occurs on particle surfaces and grain boundaries. This implies that a high surface area may hinder grain boundary enrichment of Co cations, a hypothesis that requires further validation.

Conclusions

Contrary to conventional percolation theory, which asserts that optimal conductivity necessitates the continuous connectivity of individual phases, this study establishes an alternative paradigm in which superior mixed conductivities are achieved through novel mechanisms free of strict phase percolation.

A case study exemplifying this concept involves mixed ionic and electronic conductors synthesized from Gd-doped ceria with iron–cobalt oxide additions. A superior network for simultaneous ionic and electronic conduction is successfully established by percolating additive ($FeCo_2O_4$)-induced electronic conducting grains within the ionic conductor (Gd-doped ceria) through its mixed conductive grain boundaries. The study demonstrates that percolation of the electronic conducting grains within the Gd-doped ceria matrix is not a prerequisite for achieving efficient electronic conduction, thereby significantly mitigating the ion-blocking effect.

Comprehensive structural and compositional analyses, spanning from micro-to nanoscale, reveal that the observed enhancements in conductivity are closely associated with: (1) the geometry of the percolation network, which optimizes conduction pathways; (2) the strategic segregation of iron and cobalt at ceria grain boundaries, which enhances electronic conduction. The synergistic optimizations in both ionic and electronic transport, especially under dual-atmosphere conditions, are achieved through the stabilization of the segregation, alongside the suppression of grain growth, at a significantly lowered densification temperature of 1050 °C.

The optimized MIEC delivers an excellent and sustainable oxygen permeation performance, advancing its applications in clean and efficient energy technologies.

Data availability

The data supporting this study have been included as part of the manuscript and its ESI.†

Author contributions

Fanlin Zeng: conceptualization, data curation, formal analysis, investigation, methodology, project administration, resources, software, validation, visualization, writing – original draft; Ke Ran: conceptualization, data curation, formal analysis, investigation, methodology, resources, software, validation, visualization, writing – review & editing; Christian Dellen: data curation, formal analysis, methodology, software, validation, visualization, writing – review and editing; Hartmut Schlenz: conceptualization, supervision, validation, writing – review & editing; Joachim Mayer: resources, supervision, validation, writing – review & editing; Ruth Schwaiger: resources, supervision, validation, writing – review & editing; Wilhelm Albert Meulenberg:

resources, supervision, validation, writing – review & editing; Stefan Baumann: conceptualization, data curation, formal analysis, investigation, methodology, project administration, resources, software, supervision, validation, visualization, writing – review & editing.

Conflicts of interest

There are no conflicts to declare.

References

1 K.-D. Kreuer, *Chem. Mater.*, 2014, **26**, 361–380.
2 N. Devi, B. Singh and S.-J. Song, in *Advanced Ceramics for Versatile Interdisciplinary Applications*, ed. S. Singh, P. Kumar and D. P. Mondal, Elsevier, 2022, pp. 201–230, DOI: 10.1016/B978-0-323-89952-9.00007-5.
3 X. Dong, W. Jin, N. Xu and K. Li, *Chem. Commun.*, 2011, **47**, 10886–10902.
4 L. Jia, G. He, Y. Zhang, J. Caro and H. Jiang, *Angew. Chem., Int. Ed.*, 2021, **60**, 5204–5208.
5 H. Jiang, H. Wang, S. Werth, T. Schiestel and J. Caro, *Angew. Chem., Int. Ed.*, 2008, **47**, 9341–9344.
6 W. Fang, F. Steinbach, Z. Cao, X. Zhu and A. Feldhoff, *Angew. Chem., Int. Ed.*, 2016, **55**, 8648–8651.
7 S. C. Singhal, *MRS Bull.*, 2000, **25**, 16–21.
8 S. Baumann, J. M. Serra, M. P. Lobera, S. Escolástico, F. Schulze-Küppers and W. A. Meulenberg, *J. Membr. Sci.*, 2011, **377**, 198–205.
9 J. M. Serra, J. Garcia-Fayos, S. Baumann, F. Schulze-Küppers and W. A. Meulenberg, *J. Membr. Sci.*, 2013, **447**, 297–305.
10 M. Schulz, R. Kriegel and A. Kämpfer, *J. Membr. Sci.*, 2011, **378**, 10–17.
11 J. Gao, L. Li, Z. Yin, J. Zhang, S. Lu and X. Tan, *J. Membr. Sci.*, 2014, **455**, 341–348.
12 S. Pirou, J. M. Bermudez, B. T. Na, S. Ovtar, J. H. Yu, P. V. Hendriksen, A. Kaiser, T. R. Reina, M. Millan and R. Kiebach, *J. Membr. Sci.*, 2018, **552**, 115–123.
13 S. Pirou, J. García-Fayos, M. Balaguer, R. Kiebach and J. M. Serra, *J. Membr. Sci.*, 2019, **580**, 307–315.
14 V. V. Kharton, F. M. B. Marques and A. Atkinson, *Solid State Ionics*, 2004, **174**, 135–149.
15 C. Zhang, J. Sunarso and S. Liu, *Chem. Soc. Rev.*, 2017, **46**, 2941–3005.
16 M. Ramasamy, E. S. Persoon, S. Baumann, M. Schroeder, F. Schulze-Küppers, D. Görtz, R. Bhave, M. Bram and W. A. Meulenberg, *J. Membr. Sci.*, 2017, **544**, 278–286.
17 J. H. Park and R. N. Blumenthal, *J. Electrochem. Soc.*, 1989, **136**, 2867.

14954 | *J. Mater. Chem. A*, 2025, **13**, 14940–14956

This journal is © The Royal Society of Chemistry 2025

18 S. Wang, T. Kobayashi, M. Dokiya and T. Hashimoto, *J. Electrochem. Soc.*, 2000, **147**, 3606.

19 C. Chatzichristodoulou and P. V. Hendriksen, *J. Electrochem. Soc.*, 2012, **159**, E162.

20 D. Ramasamy, A. L. Shaula, A. Gómez-Herrero, V. V. Kharton and D. P. Fagg, *J. Membr. Sci.*, 2015, **475**, 414–424.

21 P. Shuk and M. Greenblatt, *Solid State Ionics*, 1999, **116**, 217–223.

22 V. Esposito, D. Z. de Florio, F. C. Fonseca, E. N. S. Muccillo, R. Muccillo and E. Traversa, *J. Eur. Ceram. Soc.*, 2005, **25**, 2637–2641.

23 H. Takamura, H. Sugai, M. Watanabe, T. Kasahara, A. Kamegawa and M. Okada, *J. Electroceram.*, 2006, **17**, 741–748.

24 S. Cheng, M. Søgaard, L. Han, W. Zhang, M. Chen, A. Kaiser and P. V. Hendriksen, *Chem. Commun.*, 2015, **51**, 7140–7143.

25 M. Balaguer, J. García-Fayos, C. Solís and J. M. Serra, *Chem. Mater.*, 2013, **25**, 4986–4993.

26 H. Luo, H. Jiang, K. Efimov, F. Liang, H. Wang and J. r. Caro, *Ind. Eng. Chem. Res.*, 2011, **50**, 13508–13517.

27 Y. Lin, S. Fang, D. Su, K. S. Brinkman and F. Chen, *Nat. Commun.*, 2015, **6**, 6824.

28 F. Zeng, J. Malzbender, S. Baumann, M. Krüger, L. Winnubst, O. Guillon and W. A. Meulenberg, *J. Eur. Ceram. Soc.*, 2020, **40**, 5646–5652.

29 D. P. Fagg, V. V. Kharton and J. R. Frade, *J. Electroceram.*, 2002, **9**, 199–207.

30 D. P. Fagg, J. C. C. Abrantes, D. Pérez-Coll, P. Núñez, V. V. Kharton and J. R. Frade, *Electrochim. Acta*, 2003, **48**, 1023–1029.

31 S. Taub, R. E. A. Williams, X. Wang, D. W. McComb, J. A. Kilner and A. Atkinson, *Acta Mater.*, 2014, **81**, 128–140.

32 C. Lenser, F. Gunkel, Y. J. Sohn and N. H. Menzler, *Solid State Ionics*, 2018, **314**, 204–211.

33 K. Ran, L. Fischer, S. Baumann, W. A. Meulenberg, K. Neuhaus and J. Mayer, *Acta Mater.*, 2022, **226**, 117603.

34 F. Zeng, S. Baumann, J. Malzbender, A. Nijmeijer, L. Winnubst, O. Guillon, R. Schwaiger and W. A. Meulenberg, *J. Membr. Sci.*, 2021, **628**, 119248.

35 K. Ran, F. Zeng, L. Fischer, S. Baumann, W. A. Meulenberg, K. Neuhaus and J. Mayer, *Acta Mater.*, 2022, **234**, 118034.

36 F. Zeng, J. Malzbender, S. Baumann, A. Nijmeijer, L. Winnubst, M. Ziegner, O. Guillon, R. Schwaiger and W. A. Meulenberg, *J. Eur. Ceram. Soc.*, 2021, **41**, 509–516.

37 A. J. Schwartz, M. Kumar, B. L. Adams and D. P. Field, *Electron Backscatter Diffraction in Materials Science*, Springer, New York, USA, 2009.

38 J. T. Gostick, Z. A. Khan, T. G. Tranter, M. D. Kok, M. Agnaou, M. Sadeghi and R. Jervis, *J. Open Source Softw.*, 2019, **4**, 1296.

39 A. Kovács, R. Schierholz and K. Tillmann, *J. Large-Scale Res. Facil.*, 2016, **2**, A43.

40 K. Ran, W. Deibert, M. E. Ivanova, W. A. Meulenberg and J. Mayer, *Nanoscale*, 2020, **12**, 17841–17848.

41 M. Ramasamy, S. Baumann, J. Palisaitis, F. Schulze-Küppers, M. Balaguer, D. Kim, W. A. Meulenberg, J. Mayer, R. Bhave, O. Guillon and M. Bram, *J. Am. Ceram. Soc.*, 2016, **99**, 349–355.

42 F. Zeng, J. Malzbender, S. Baumann, W. Zhou, M. Ziegner, A. Nijmeijer, O. Guillon, R. Schwaiger and W. A. Meulenberg, *J. Am. Ceram. Soc.*, 2021, **104**, 1814–1830.

43 T.-T. Nguyen, A. Demortière, B. Fleutot, B. Delobel, C. Delacourt and S. J. Cooper, *npj Comput. Mater.*, 2020, **6**, 123.

44 J. Landesfeind, J. Hattendorff, A. Ehrl, W. A. Wall and H. A. Gasteiger, *J. Electrochem. Soc.*, 2016, **163**, A1373.

45 C. A. Schneider, W. S. Rasband and K. W. Eliceiri, *Nat. Methods*, 2012, **9**, 671–675.

46 J. Bae, Y. Lim, J.-S. Park, D. Lee, S. Hong, J. An and Y.-B. Kim, *J. Electrochem. Soc.*, 2016, **163**, F919.

47 Y. Lei, Y. Ito, N. D. Browning and T. J. Mazanec, *J. Am. Ceram. Soc.*, 2002, **85**, 2359–2363.

48 Z.-P. Li, T. Mori, G. J. Auchterlonie, J. Zou and J. Drennan, *Appl. Phys. Lett.*, 2011, **98**, 093104.

49 B. Feng, T. Yokoi, A. Kumamoto, M. Yoshiya, Y. Ikuhara and N. Shibata, *Nat. Commun.*, 2016, **7**, 11079.

50 D. Pérez-Coll, P. Núñez, J. C. C. Abrantes, D. P. Fagg, V. V. Kharton and J. R. Frade, *Solid State Ionics*, 2005, **176**, 2799–2805.

51 Z. Zhang, W. Sigle, M. Rühle, E. Jud and L. J. Gauckler, *Acta Mater.*, 2007, **55**, 2907–2917.

52 H. Hojo, T. Mizoguchi, H. Ohta, S. D. Findlay, N. Shibata, T. Yamamoto and Y. Ikuhara, *Nano Lett.*, 2010, **10**, 4668–4672.

53 K. Song, H. Schmid, V. Srot, E. Gilardi, G. Gregori, K. Du, J. Maier and P. A. van Aken, *APL Mater.*, 2014, **2**, 032104.

54 P. Yan, T. Mori, Y. Wu, Z. Li, G. J. Auchterlonie, J. Zou and J. Drennan, *Microsc. Microanal.*, 2013, **19**, 102–110.

55 W. J. Bowman, J. Zhu, R. Sharma and P. A. Crozier, *Solid State Ionics*, 2015, **272**, 9–17.

56 E. V. Tsipis, J. C. Waerenborgh and V. V. Kharton, *J. Solid State Electrochem.*, 2017, **21**, 2965–2974.

57 X. Guo and R. Waser, *Solid State Ionics*, 2004, **173**, 63–67.

58 D. R. Diercks, J. Tong, H. Zhu, R. Kee, G. Baure, J. C. Nino, R. O'Hayre and B. P. Gorman, *J. Mater. Chem. A*, 2016, **4**, 5167–5175.

59 M. A. Frechero, M. Rocci, G. Sánchez-Santolino, A. Kumar, J. Salafranca, R. Schmidt, M. R. Díaz-Guillén, O. J. Durá, A. Rivera-Calzada, R. Mishra, S. Jesse, S. T. Pantelides, S. V. Kalinin, M. Varela, S. J. Pennycook, J. Santamaria and C. Leon, *Sci. Rep.*, 2015, **5**, 17229.

60 C. Tian and S.-W. Chan, *Solid State Ionics*, 2000, **134**, 89–102.

61 P.-L. Chen and I. W. Chen, *J. Am. Ceram. Soc.*, 1996, **79**, 1793–1800.

62 D. R. Ou, T. Mori, F. Ye, J. Zou, G. Auchterlonie and J. Drennan, *Phys. Rev. B:Condens. Matter Mater. Phys.*, 2008, **77**, 024108.

63 W. J. Bowman, M. N. Kelly, G. S. Rohrer, C. A. Hernandez and P. A. Crozier, *Nanoscale*, 2017, **9**, 17293–17302.

64 J. Kim, S. Im, S. H. Oh, J. Y. Lee, K. J. Yoon, J.-W. Son, S. Yang, B.-K. Kim, J.-H. Lee, H.-W. Lee, J.-H. Lee and H.-I. Ji, *Sci. Adv.*, 7, eabj8590.

65 M. Machado, A. L. da Silva, L. P. R. Moraes, L. N. Rodrigues, L. B. Caliman, D. Gouvêa and F. C. Fonseca, *CrystEngComm*, 2023, **25**, 6102–6110.

This journal is © The Royal Society of Chemistry 2025

J. Mater. Chem. A, 2025, **13**, 14940–14956 | **14955**

66 X. Guo and R. Waser, *Prog. Mater. Sci.*, 2006, **51**, 151–210.

67 A. Tschöpe, *Solid State Ionics*, 2001, **139**, 267–280.

68 R. Tanaka, W. S. Oliveira, A. Brandão, J. C. C. Abrantes and J. R. Frade, *Electrochim. Acta*, 2012, **85**, 116–121.

69 E.-J. Yi, M.-Y. Yoon, J.-W. Moon and H.-J. Hwang, *J. Korean Ceram. Soc.*, 2010, **47**, 199–190.

70 P. Seeharaj, A. Berenov, E. Raj, R. Rudkin and A. Atkinson, *Solid State Ionics*, 2011, **192**, 638–641.

71 X. Zhu, M. Li, H. Liu, T. Zhang, Y. Cong and W. Yang, *J. Membr. Sci.*, 2012, **394–395**, 120–130.

72 S. R. Bishop, T. S. Stefanik and H. L. Tuller, *Phys. Chem. Chem. Phys.*, 2011, **13**, 10165–10173.

73 E. Y. Pikalova, A. N. Demina, A. K. Demin, A. A. Murashkina, V. E. Sopernikov and N. O. Esina, *Inorg. Mater.*, 2007, **43**, 735–742.

74 B. Aktas and S. Tekeli, *Int. J. Mater. Res.*, 2014, **105**, 577–583.

75 N. W. Kwak, D.-K. Lim, S. J. Jeong, P. Byeon, S.-Y. Chung and W. Jung, *Adv. Mater. Interfaces*, 2020, **7**, 2000688.

76 T. Zhang, L. Kong, Z. Zeng, H. Huang, P. Hing, Z. Xia and J. Kilner, *J. Solid State Electrochem.*, 2003, **7**, 348–354.

77 S.-H. Park and H.-I. Yoo, *Solid State Ionics*, 2005, **176**, 1485–1490.

78 S. Taub, K. Neuhaus, H.-D. Wiemhöfer, N. Ni, J. A. Kilner and A. Atkinson, *Solid State Ionics*, 2015, **282**, 54–62.

79 M. Izuki, M. E. Brito, K. Yamaji, H. Kishimoto, D.-H. Cho, T. Shimonosono, T. Horita and H. Yokokawa, *J. Power Sources*, 2011, **196**, 7232–7236.

80 Z.-P. Li, M. Toshiyuki, G. J. Auchterlonie, J. Zou and D. John, *ACS Appl. Mater. Interfaces*, 2011, **3**, 2772–2778.

81 A. Shaula, V. Kharton, F. Marques, A. Kovalevsky, A. Viskup and E. Naumovich, *J. Solid State Electrochem.*, 2006, **10**, 28–40.

82 V. Kharton, A. Kovalevsky, A. Viskup, A. Shaula, F. Figueiredo, E. Naumovich and F. Marques, *Solid State Ionics*, 2003, **160**, 247–258.

83 J. H. Joo, G. S. Park, C.-Y. Yoo and J. H. Yu, *Solid State Ionics*, 2013, **253**, 64–69.

84 E. Jud and L. J. Gauckler, *J. Electroceram.*, 2005, **14**, 247–253.

14956 | *J. Mater. Chem. A*, 2025, **13**, 14940–14956

This journal is © The Royal Society of Chemistry 2025